Draft: Version 5 — LaTeXed on April 25, 2011

GRB 081029: A Gamma-Ray Burst with a Multi-Component Afterglow

Stephen T. Holland[1,2,3], Massimiliano De Pasquale[4], Jirong Mao[5,6,7,8], Taka Sakamoto[1,9,3], Patricia Schady[10,4], Stefano Covino[5], Yi-Zhong Fan[11], Zhi-Ping Jin[5,11], Paolo D'Avanzo[5], Angelo Antonelli[12], Valerio D'Elia[12], Guido Chincarini[5], Fabrizio Fiore[12], Shashi Bhushan Pandey[13,14]

ABSTRACT

[1]Astrophysics Science Division, Code 660.1, 8800 Greenbelt Road Goddard Space Flight Centre, Greenbelt, MD 20771 U.S.A.

Stephen.T.Holland@nasa.gov

[2]Universities Space Research Association 10211 Wincopin Circle, Suite 500 Columbia, MD 21044 U.S.A.

[3]Centre for Research and Exploration in Space Science and Technology Code 668.8 8800 Greenbelt Road Goddard Space Flight Centre, Greenbelt, MD 20771 U.S.A.

[4]Mullard Space Science Laboratory, University College London, Holmbury St Mary, Dorking Surrey RH5 6NT, UK

[5]INAF-Osservatorio Astronomico di Brera, Via Emilio Bianchi 46, I–23807 Merate (LC), Italy

[6]Yunnan Observatory, Chinese Academy of Sciences, Kumming, Yunan Province, 650011, China

[7]International Centre for Astrophysics, Korea Astronomy and Space Science Institute 776, Daedeokdae-ro, Yuseong-gu, Daejeon, Republic of Korea 305–348

[8]Key Laboratory for the Structure and Evolution of Celestial Objects, Chinese Academy of Sciences, Kunming, Yunnan Province, 650011, China

[9]Joint Centre for Astrophysics, University of Maryland, Baltimore County, 1000 Hilltop Circle, Baltimore, MD 21250, USA

[10]Max-Planck Institut für Extraterrestrische Physik, Giessenbachstraße, D–85748 Garching, Germany

[11]Purple Mountain Observatory, Chinese Academy of Sciences, Nanjing 210008, China

[12]INAF-Osservatorio Astronomico di Roma, Via de Frascati 33, I–00040 Monteporzio Catone (Roma), Italy

[13]Randall Laboratory of Physics, University of Michigan, 450 Church St, Ann Arbor, MI 48109–1040, USA

[14]Aryabhatta Research Institute of Observational Sciences, Manora Peak, Nainital, 263129, India

We present an analysis of the unusual optical light curve of the gamma-ray burst GRB 081029, a long–soft burst with a redshift of $z = 3.8479$. We combine X-ray and optical observations from the *Swift* X-Ray Telescope and the *Swift* UltraViolet Optical Telescope with ground-based optical and infrared data obtained using the REM and ROTSE telescopes to construct a detailed data set extending from 86 s to $\sim$100 000 s after the BAT trigger. Our data cover a wide energy range, from 10 keV to 0.77 eV (1.24 Å to 16 000 Å). The X-ray afterglow shows a shallow initial decay followed by a rapid decay starting at about 18 000 s. The optical and infrared afterglow, however, shows an uncharacteristic rise at about 5000 s that does not correspond to any feature in the X-ray light curve. Our data are not consistent with synchrotron radiation from a jet interacting with an external medium, a two-component jet, or continuous energy injection from the central engine. We find that the the optical light curves can be broadly explained by a collision between two ejecta shells within a two-component jet. A growing number of gamma-ray burst afterglows are consistent with complex jets, which suggests that some (or all) gamma-ray burst jets are complex and will require detailed modelling to fully understand them.

Subject headings: gamma rays: bursts

1. Introduction

The *Swift* observatory (Gehrels et al. 2004) is a multi-instrument satellite mission that was designed to detect and rapidly localize gamma-ray bursts (GRBs). The observatory contains three telescopes. The Burst Alert Telescope (BAT; Barthelmy et al. 2005) is used to identify GRBs and localize them to $\sim$3′ in the energy range 15–150 keV. Once BAT has localized a burst *Swift* slews to point the X-Ray Telescope (XRT; Burrows et al. 2005) and the UltraViolet/Optical Telescope (UVOT; Roming et al. 2005) at the burst. The XRT obtains X-ray localizations to $\lesssim$5″ in the energy range 0.2–10 keV while the UVOT obtains localizations to $\sim$ 0″.5 then cycles through a set of optical and ultraviolet filters covering the wavelength range from 1700 Å to 6500 Å.

The gamma-ray burst GRB 081029 was detected by the BAT at 01:43:56 UT on 2008 Oct 29. *Swift* was unable to slew immediately to this burst due to an Earth limb constraint, so the first *Swift* narrow-field observations did not begin until approximately 45 minutes after the BAT trigger. The BAT light curve showed a single smooth peak and had a T_{90} duration of 270 ± 45 s (Cummings et al. 2008). The spectrum of the prompt emission was well-fit by a simple power law.

The ROTSE-IIIc telescope located the optical afterglow of GRB 081029 86 s after the burst (Rykoff 2008). The afterglow was also detected in the infrared by the REM telescope at 154 s (Covino et al. 2008), but not in the ultraviolet (Holland & Sakamoto 2008). UVOT optical data showed a rise between approximately 2700 and 9000 s while Cobb (2008) detected the afterglow in both the optical and infrared using ANDICAM on the CTIO 1.3-m telescope. They found that the afterglow decayed with a power-law index of approximately -0.9 between about 9000 and 13 000 s after the trigger. The XRT found a fading source (Goad et al. 2008) at the ROTSE-IIIc location (Rykoff 2008). The Australia Compact Telescope Array observed GRB 081029 approximately one month after the burst at 4.800 and 4.928 GHz, but did not detect the afterglow. Their merged data at 4.800 and 4.928 GHz yielded a radio flux density, at the afterglow position, of $f_\nu = -0.168 \pm 0.219$ mJy per beam (Moin et al. 2008).

A redshift of $z = 3.8479 \pm 0.0002$ was measured from several absorption features by the VLT/UVES (D'Elia et al. 2008) and was confirmed by Gemini-South/GMOS (Cucchiara et al. 2008). The GMOS spectrum shows evidence for a damped Lyman-alpha system as well as several metal absorption features in the host galaxy.

In this paper we present space- and ground-based gamma-ray, X-ray, ultraviolet, and optical observations of GRB 081029. We will propose that the X-ray, optical, and infrared data suggest that the afterglow of GRB 081029 can broadly be explained by the collision of a fast-moving ejecta shell with a slower shell within a two-component jet.

2. Data

2.1. BAT Data

The BAT data analysis was performed using the *Swift* HEASOFT 6.5.1 software package. The burst pipeline script, BATGRBPRODUCT, was used to process the BAT event data. We used the the position of the optical afterglow source input position during the process.

Figure 1 shows the BAT energy resolved light curves of GRB 081029 with 10 s binning. The light curve shows an extremely weak and smooth profile with the T_{90} duration of 280 ± 50 s (1 σ, statistical). The 1 s peak flux in the 15–150 keV band measured in the 1 s time window starting from 20.6 s after the BAT trigger time is $(2.8 \pm 1.3) \times 10^{-8}$ erg cm^{-2} s^{-1}. The energy fluence in the 15–150 keV band is $(2.0 \pm 0.2) \times 10^{-6}$ erg cm^{-2}. The time-averaged spectrum is well fitted by a simple power law with the photon index of 1.5 ± 0.2.

Because of the weak and the smooth light curve of the prompt emission, GRB 081029

satisfies the BAT possible high-z criteria (Ukwatta et al. 2008). The BAT possible high-z criteria are basically selecting those bursts with weak, smooth light curves and hard spectra. Figure 2 shows the distributions of GRB 081029, the BAT known-z bursts which satisfy Ukwatta et al. (2008) possible BAT high-z criteria, and the BAT long GRBs in the peak flux and the fluence plane. The BAT parameters are from the BAT1 catalogue (Sakamoto et al. 2008b). As seen in the figure, GRB 081029 has the lower peak flux and fluence than the higher redshift bursts such as GRB 050904, GRB 060510B, and GRB 050814. Therefore, the weakness and the smoothness of the light curve in the prompt emission might be more related to the central engine of the burst rather than the cosmological redshift effect.

2.2. XRT Data

XRT began to observe GRB 081029 2448 s after the BAT trigger. The UVOT-enhanced X-ray position is RA, Dec = 23:07:05.51, -68:09:21.9 (J2000.0) with an uncertainty of $1''\!.5$ (radius, 90% confidence). The observational data were processed by the *Swift* Data Center at NASA/GSFC and further calibrated with XRTPIPELINE. For details of how the light curve was produced see Evans et al. (2007). All the XRT data for GRB 081029 were collected in Photon Counting (PC) mode.

The X-ray light curve can be modelled by a broken power law ($f(t) \propto t^{-\alpha}$). The best-fitting model has decay indices of $\alpha_{X,1} = 0.56 \pm 0.03$ and $\alpha_{X,2} = 2.56 \pm 0.09$ with a break time of $t_{X,b} = 18\,230 \pm 346$ s yielding a goodness-of-fit of $\chi^2/\mathrm{dof} = 93.947/77 = 1.22$. The X-ray light curve with this fit is shown in Figure 3. Alternately, if we fit a smoothly-varying broken power law (Beuermann et al. 1999) we find $\alpha_{X,1} = 0.45 \pm 0.11$, $\alpha_{X,2} = 2.65 \pm 0.23$, and a smoothness parameter of $n = 2.3 \pm 1.5$ with $\chi^2/\mathrm{dof} = 91.260/76 = 1.20$. The initial X-ray light curve shows some evidence for flaring between approximately 2500 and 5000 s after the BAT trigger. The sawtooth behaviour of the X-ray emission during this period is consistent with flares with $\Delta t/t \lesssim 1$. It is possible that the X-ray photons that we see at this time are due to flaring on top of a power law decay. The lack of X-ray data before 2000 s could be causing us to miss the rise of the flare and thus give the impression that the X-ray photons seen between 2000 s and 5000 s are due solely to the plateau phase of the X-ray light curve.

The X-ray spectrum can be fit by an absorbed power law with a photon index $\Gamma_X = 1.98 \pm 0.08$, corresponding to $\beta_X = 0.98 \pm 0.08$. The assumed Galactic column density value in the direction of the burst is $N_H = 2.8 \times 10^{20}$ cm^{-2} (Kalberla et al. 2005) and the fitted intrinsic column density in the host galaxy is $N_H = 4.9^{+3.9}_{-2.7} \times 10^{21}$ cm^{-2}. Assuming an SMC-like relation between the neutral hydrogen column density and the V-band extinction
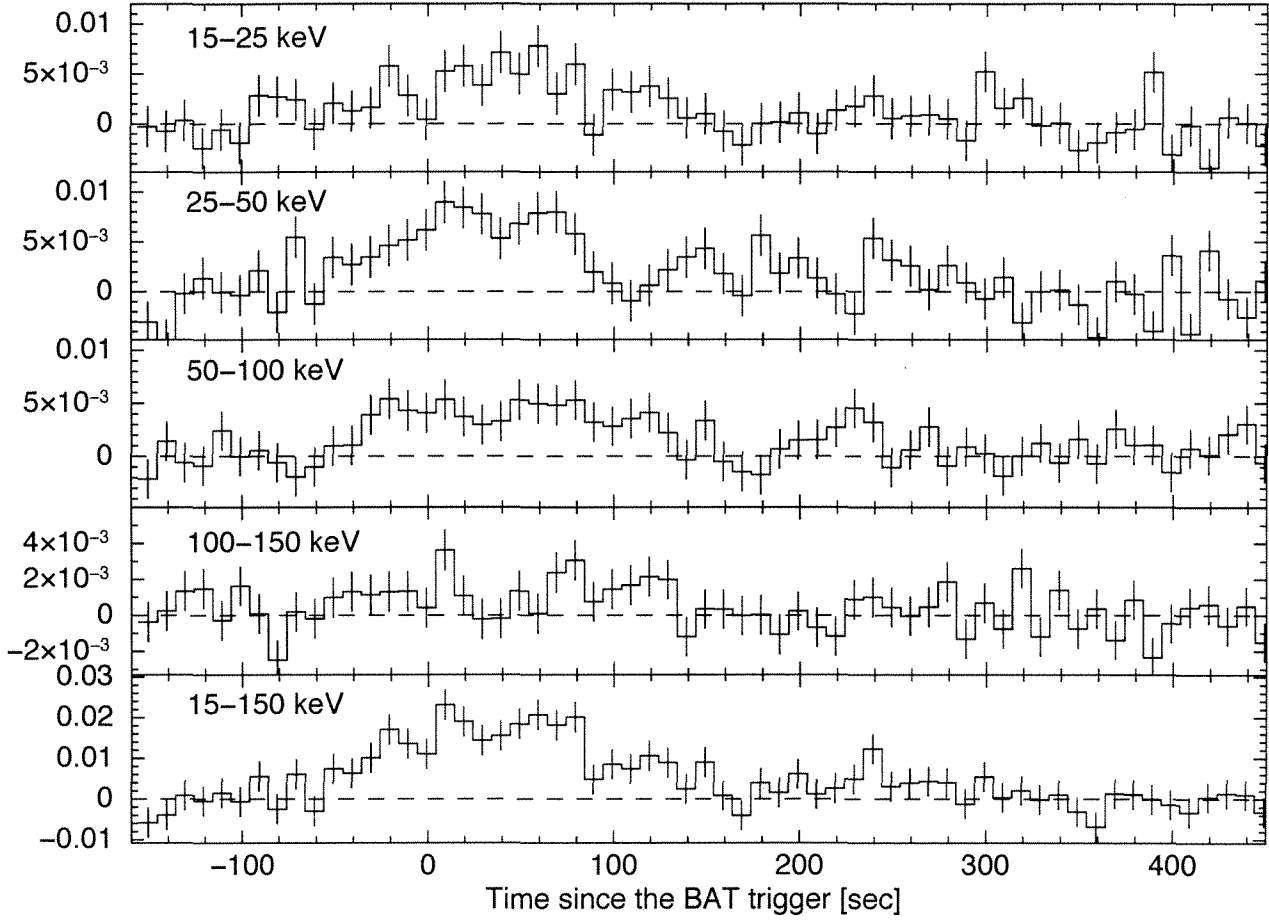
Fig. 1.— The BAT energy resolved light curves of GRB 081029 with 10 s binning.
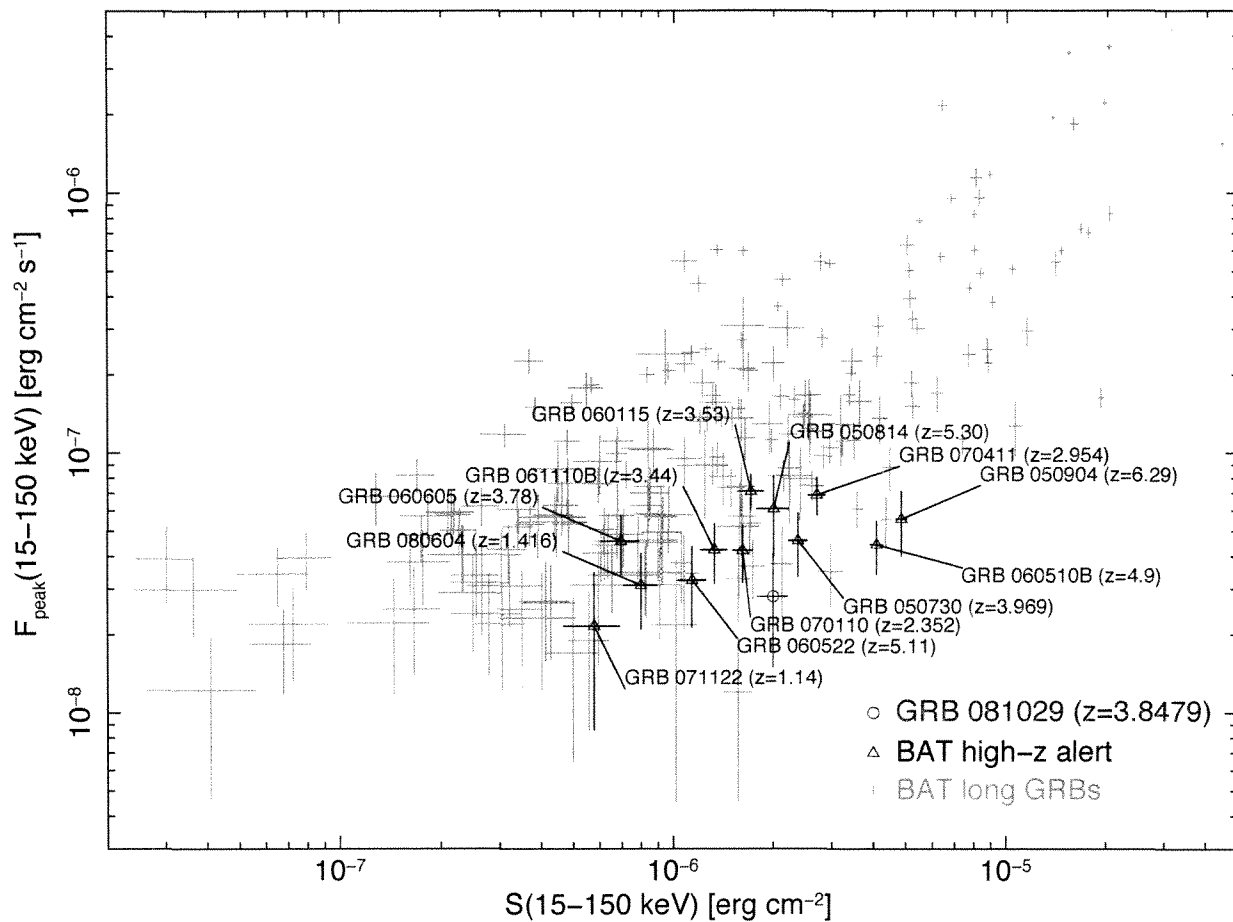
Fig. 2.— Distribution of the 1 s peak energy flux in the 15–150 keV band versus the energy fluence in the 15–150 keV band. GRB 081029 is indicated with a red circle. BAT GRBs with known redshifts that satisfy the Ukwatta et al. (2008) high-z criteria are indicated with blue triangles, and BAT long GRBs are shown with gray crosses.
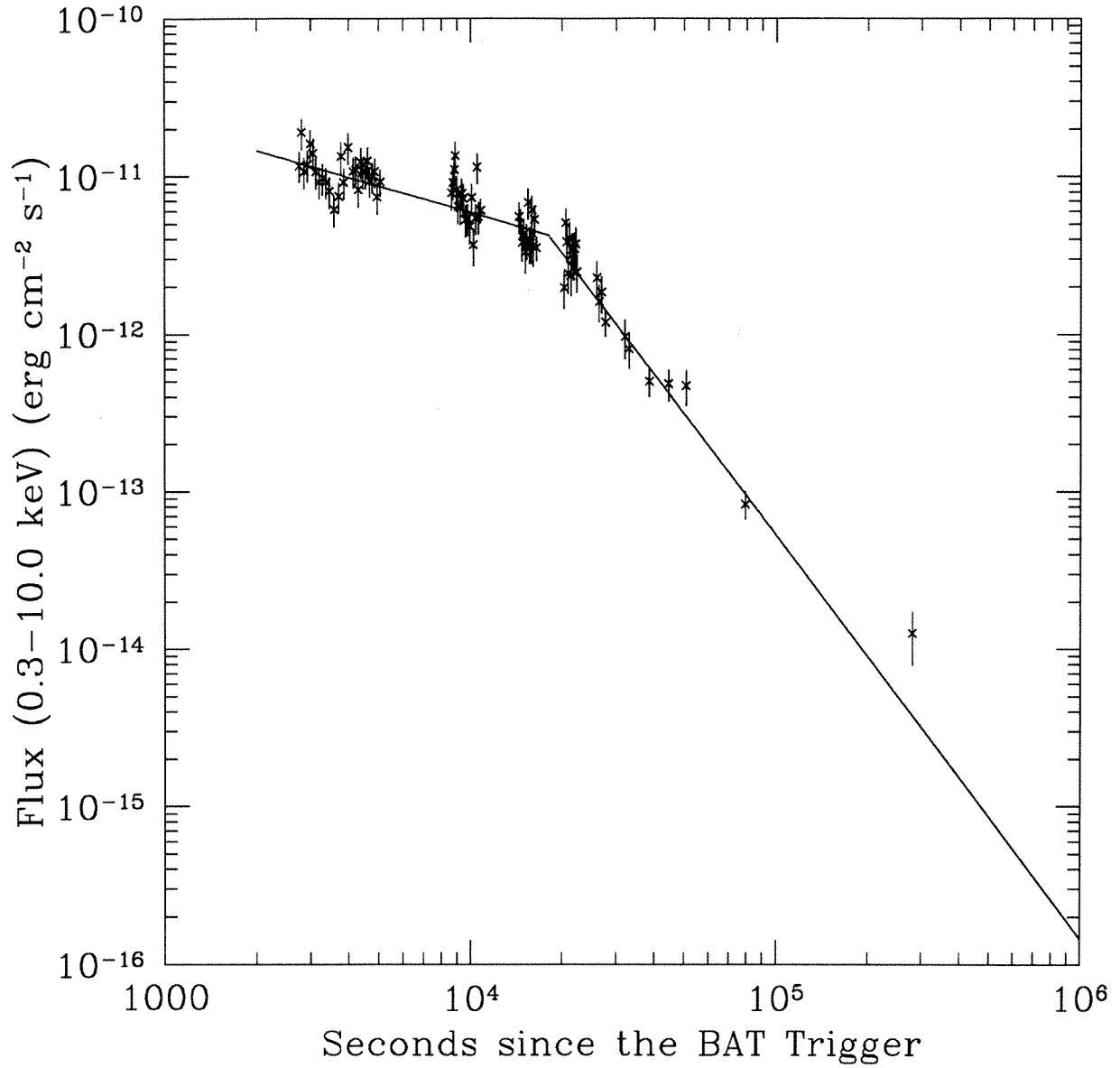
Fig. 3.— This Figure shows the *Swift*/XRT light curve. The last point is a 3-σ upper limit. The data have not been corrected for Galactic absorption or absorption in the host galaxy.

of $N_H = (15.4 \times 10^{21})A_V$ (equation (4) and Table 2 of Pei 1992) this corresponds to $A_V = 0.3^{+0.3}_{-0.2}$ mag in the rest frame of the host galaxy. However, the observed gas-to-dust ratio for GRB host galaxies varies by about a factor of ten (Schady et al. 2007), so the X-ray data alone can only constrain the rest frame V-band extinction to be $A_V \lesssim 2$ mag. The observed 0.3–10 keV flux is 3.1×10^{-12} erg cm^{-2} s^{-1}, which corresponds to an unabsorbed value of $\sim 3.5 \times 10^{-12}$ erg cm^{-2} s^{-1}. This was computed using the time-average spectrum between 2.7×10^3 s and 6.2×10^4 s after the BAT trigger.

2.3. UVOT Data

The *Swift*/UVOT began settled observations 2708 s after the BAT trigger (Sakamoto et al. 2008a). An optical afterglow was detected in the initial white exposure with a magnitude of $20.51^{-0.30}_{+0.41}$. The afterglow increased in luminosity until approximately 9000 s and then faded. The UVOT position of the afterglow is RA, Dec = 23:07:05.32, −68:09:19.7 with an estimated internal uncertainty of $0\rlap{.}''24$ and an estimated systematic uncertainty relative to the ICRS (Fey et al. 2004) of $0\rlap{.}''42$ (Breeveld et al. 2010). These uncertainties are the 90% confidence intervals. This corresponds to Galactic coordinates of $\ell^{II}, b^{II} = 316\rlap{.}°5830, -46\rlap{.}°1091$. The field of GRB 081029 is shown in Figure 4. The afterglow is well-isolated from other sources in the field, so there is no contamination from neighbouring sources when doing aperture photometry.

We obtained the UVOT data from the *Swift* Data Archive[1]. These data have had bad pixels identified, mod-8 noise corrected, and have been transformed into FK5 coordinates. We used the standard UVOT data analysis software distributed with HEASOFT 6.9 along with the standard calibration data. Photometry was done using UVOTSOURCE with circular aperture of radius $2\rlap{.}''5$ and a nearby circular backround region with a radius of $10''$. The background region was selected to have similar background properties to those at the location of the afterglow, and to be free of contaminating sources. The UVOT photometry is presented in Table 1. The photometry was calibrated to the UVOT photometric system described in Poole et al. (2008). We have followed the Poole et al. (2008) convention and used lowercase letters to identify the UVOT bandpasses. Figure 5 shows the UVOT light curves for filters where a detection was found.

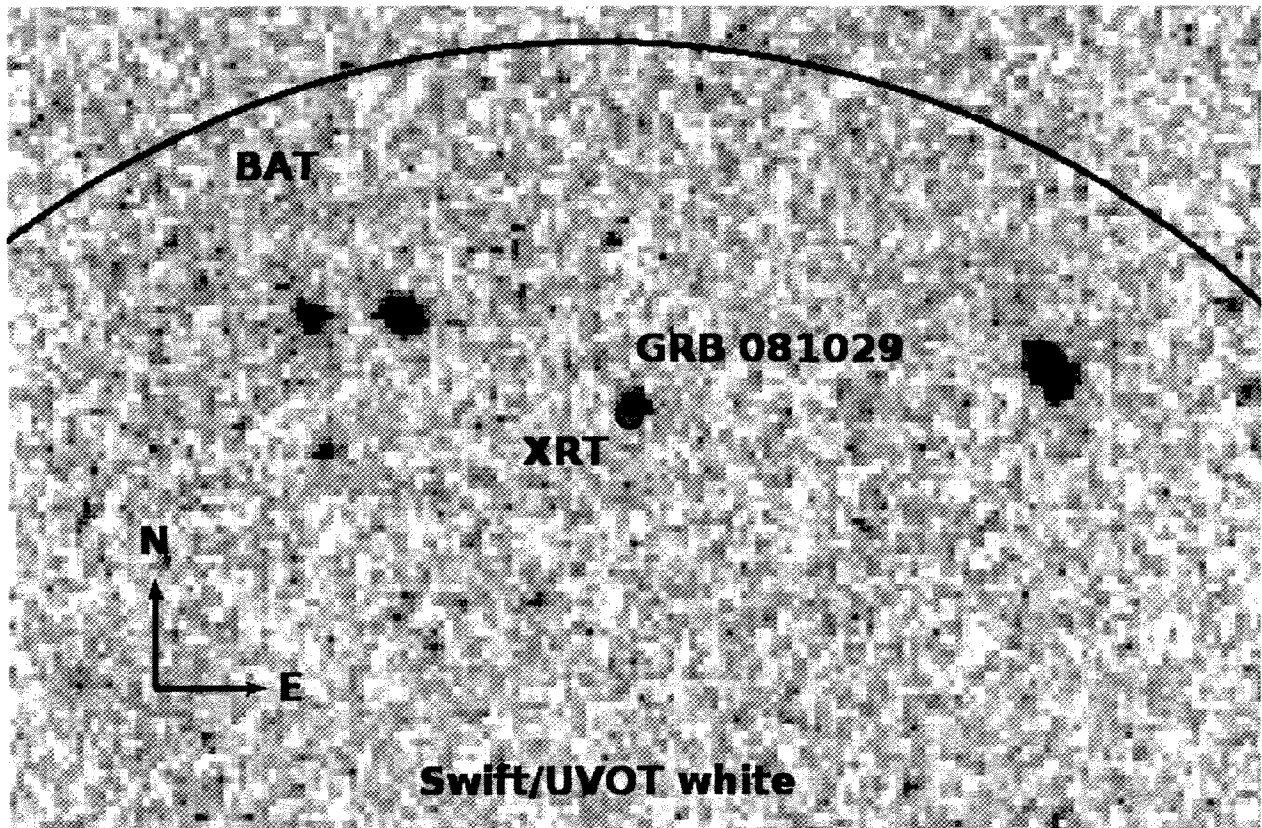[1] The *Swift* Data Archive is hosted by HEASARC.

Fig. 4.— This Figure shows a *Swift*/UVOT white image of the field of GRB 081029. The BAT and XRT error circles are shown. The XRT error circle has a radius of $1\overset{''}{.}5$. The arms of the compass have a length of 15 arcseconds.
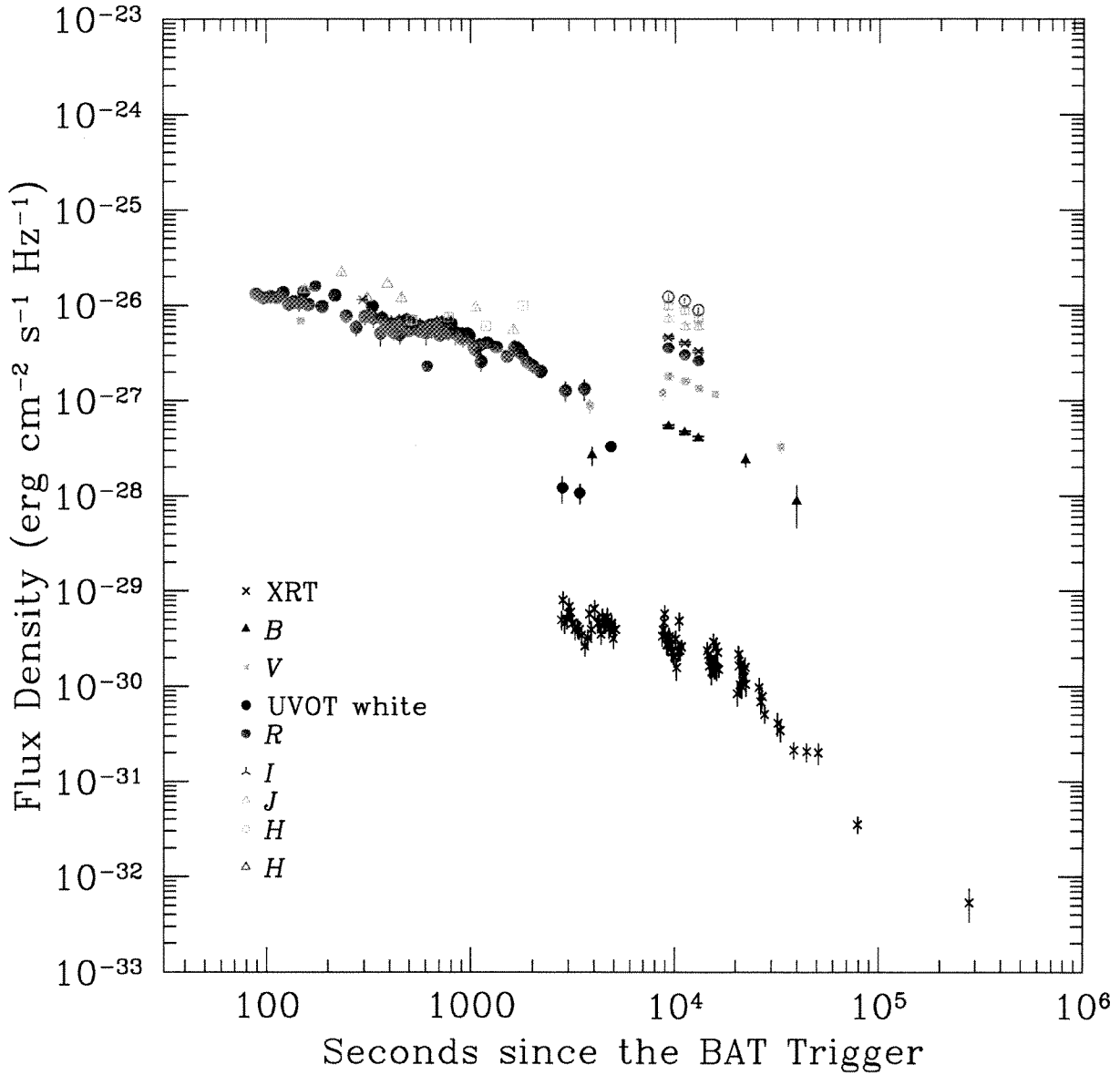
Fig. 5.— This Figure shows the flux density light curves for the X-ray data (black crosses) and the optical and infrared data. The optical/infrared photometry has not been corrected for Galactic extinction along the line of site to the burst, and the Z-ray data have not been corrected for Galactic absorption. The vertical bars represent one-sided, 1-σ error bars in the flux density. In most cases the error bars are smaller than the plotting symbol.

2.4. Ground-Based Data

2.4.1. REM Data

Observations of the afterglow of GRB 081029 were carried out with the REM telescope (Zerbi et al. 2001; Chincarini et al. 2003; Covino et al. 2004) equipped with the ROSS optical spectrograph/imager and the REMIR near-infrared camera on 2008 Oct 29, starting about 154 seconds after the burst (Covino et al. 2008). The night was clear, with a seeing of about 2″.0. We collected images with typical exposure times from 5 to 120 seconds, covering a time interval of about 0.5 hours. The complete observing log is presented in Table 2.

Image reduction was carried out by following the standard procedures: subtraction of an averaged dark frame, then division by a normalized flat. For the near-infrared data an average sky value was subtracted before dividing by the flat field. Astrometry was performed using the USNO-B1.0[2] and the 2MASS[3] catalogues. We performed aperture photometry with the SEXTRACTOR package (Bertin & Arnouts 1996) for all the objects in the field. In order to minimize any systematic effect, we performed differential photometry with respect to a selection of local isolated and non-saturated comparison stars.

In our first H- and R-band images we could detect the optical and NIR afterglow identified by Rykoff (2008) and Clemens et al. (2008) at the following coordinates: RA, Dec = 23:07:05.33, −68:09:20.0 (J2000.0 with a 1-σ error of 0″.3). Our data are given in Table 2 and shown in Figure 5. The power-law decay indices are $\alpha_H = 0.35 \pm 0.15$ (ignoring the last point), $\alpha_J = 0.50 \pm 0.04$, and $\alpha_R = 0.63 \pm 0.07$ in the H, J, and R-band, respectively. The scatter seen in the REM J-band data, and to a lesser degree the R-band data, are consistent with flaring of duration $\Delta t/t \approx 1$. The amount of scatter corresponds to a change in the flux of $\approx$10%–50%, which is similar to what is seen in the X-rays between $\approx$2500 s and 5000 s. There is no evidence for similar flaring in the optical or infrared data after $\approx$10 000 s.

2.4.2. ROTSE Data

GRB 081029 was observed by ROTSE-IIIc located at the H.E.S.S. site at Mt. Gamsberg, Namibia, for approximately 17 hr starting 86.0 s after the BAT trigger (Rykoff 2008). The ROTSE observations were taken unfiltered, but the CCD's quantum efficiency peaks at about the R band and the magnitudes were calibrated against USNO-B stars. Therefore,

---

[2]http://www.nofs.navy.mil/data/fchpix/

[3]http://www.ipac.caltech.edu/2mass/

the ROTSE magnitudes are essentially equivalent to R_c-band magnitudes. The raw images were processed using the standard ROTSE software pipeline and photometry was performed on co-added images using the method described in Quimby et al. (2006). Table 3 lists the ROTSE observations of the afterglow of GRB 081029, and they are plotted in Figure 5.

2.4.3. UVES Spectrum

The GRB 081029 optical afterglow was observed with the high resolution UV-visual echelle spectrograph (UVES; Dekker et al. 2000), mounted on the VLT-UT2 telescope, in the framework of the ESO program 082.A-0755. Observations began on 2008 Oct 29 at 02:06:37 UT ($\sim$ 23 min after the *Swift*/BAT trigger), when the magnitude of the afterglow was $R \sim 18$. Two UVES exposures of 5 and 10 minutes were obtained using both the blue and the red arms. The slit width was set to $1''$ (corresponding to a resolution of $R = 40\,000$) and the read-out mode was rebinned to 2×2 pixels. The spectral range of our observation is ~ 3300 Å to ~ 9500 Å.

The data reduction was performed using the UVES pipeline (version 2.9.7; Ballester et al. 2000). Due to the faintness of the target, the decaying magnitude during the observations, and the exposure times, the signal-to-noise ratio (S/N) was not high enough to study line variability. The S/N of the combined spectrum is ~ 3–4, allowing the identification of the main spectral features, but not a reliable estimation of their column densities. A portion of the UVES spectrum with a collection of absorption features is shown in Figure 6.

2.5. Extinction

The line-of-sight Galactic extinction in the direction of GRB 081029 is $E_{B-V} = 0.03 \pm 0.01$ mag (Schlegel et al. 1998). Using the extinction law given in Roming et al. (2009) yields extinctions in the UVOT filters of $A_v = 0.09$, $A_b = 0.12$, $A_u = 0.15$, $A_{uvw1} = 0.20$, $A_{uvm2} = 0.28$, and $A_{uvw2} = 0.25$, and $A_{white} = 0.13$ mag. For the ground-based data we adopted the Schlegel et al. (1998) extinction values of $A_R = 0.08$, $A_J = 0.03$, and $A_H = 0.02$ mag in this direction.
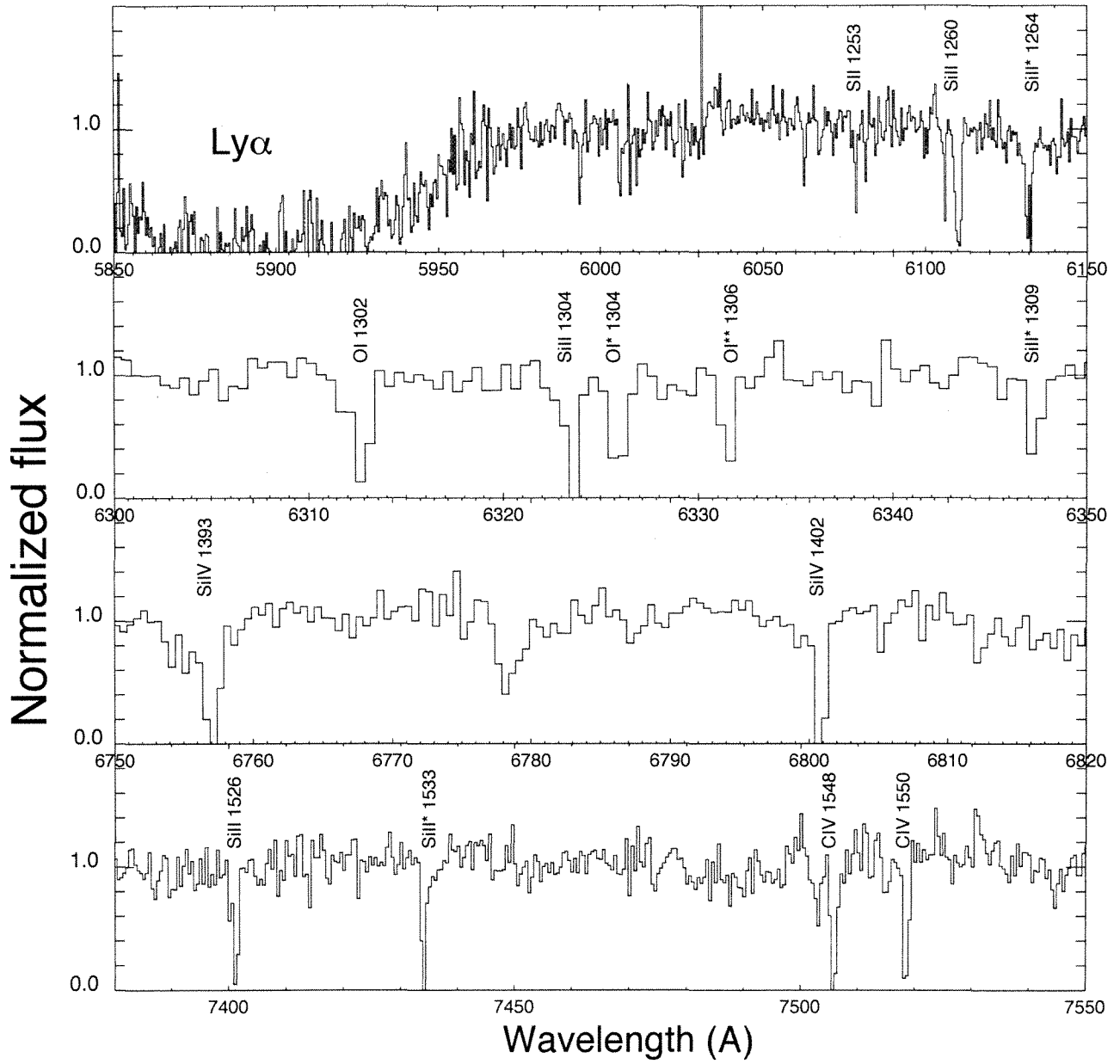
Fig. 6.— UVES spectrum of the optical afterglow of GRB 081029 showing details of the absorption system.

3. Results

3.1. Spectral Energy Distribution

Spectral energy distribution (SED) for GRB 081029 were produced at three epochs. The first SED was constructed for $T + 3000$ s using data between 3000 s and 5000 s after the BAT trigger. This epoch had X-ray data and UVOT b- and v-band data and corresponds to the period when the optical flux was rising. The second SED was constructed for $T + 12\,000$ s using data between 9000 s and 14\,000 s. This epoch had X-ray and the ground-based $RIJHK$ (Cobb 2008) data and corresponds to the period when the optical flux was near its peak. The final SED was computed for $T + 20\,000$ s using data between 15\,000 s and 25\,000 s after the BAT trigger. This epoch had X-ray and UVOT b- and v-band data and corresponds to the decay after the peak optical flux. Data were interpolated to a common time within each epoch using the observed light curves for each filter during the appropriate epoch.

We used UVOT2PHA v1.3 to convert UVOT image data to spectral files compatible with the spectral fitting package XSPEC. Version 104 of the UVOT response matrix calibration was adopted for the responsivity curves. For the ground based data, spectral files were produced for each filter using the appropriate responsivity curves and setting the magnitude to those determined from the light curve interpolations. R and I responsivity curves were taken from Bessell (1990), and the J, H and K band responsivity curves were taken from Cohen et al. (1992a,b) and Bessell et al. (1998).

XRT spectra were extracted within XSELECT (v2.4) over the 0.3–10 keV energy range. Source counts were extracted from a circular region centered on the source with a $50''$ radius, and the background count rate was measured from a circular, source-free area in the field of view, with a $150''$ radius. The spectral files were grouped to ≥ 20 counts per energy channel. Effective area files corresponding to the spectral files were created using the XRTMKARF tool (v0.5.6), where the exposure map was taken into account in order to correct for hot columns. Response matrices from version 10 of the XRT calibration files were used. The spectrum was normalized to correspond to the 0.3–10 keV flux of the X-ray afterglow at the epoch of the SED. The normalization was determined from the best-fit power-law decay model to the afterglow light curve, in the same way as was done for the UVOT and ground-based data.

The SEDs were fit using XSPEC (v12.4.0), first using a single power-law and then using a broken power-law spectral model. In both the power-law and broken power-law models two independent dust and gas components were included to correspond to the Galactic and the host galaxy photoelectric absorption and dust extinction, where the Galactic components were frozen to the column density and reddening values taken from Kalberla et al. (2005) and Schlegel et al. (1998), respectively. The dependence of the dust extinction on wavelength in

the GRB host galaxy was modelled on the Milky Way (MW), the Large Magellanic Clouds (LMC) and the Small Magellanic Clouds (SMC) empirical extinction laws using the XSPEC model ZDUST, which is based on the extinction coefficients and extinction laws from Pei (1992). The total-to-selective extinction, $R_V = A_V/E_{B-V}$ was taken to be $R_V = 3.08$, 2.93, and 3.16 for the Galactic, SMC and LMC extinction laws, respectively (Pei 1992). The equivalent neutral hydrogen column density in the host galaxy was determined from the soft X-ray absorption, where solar abundances were assumed.

To model the Lyman series absorption in the 912–1215 Å rest-frame wavelength range, we used the prescription provided in Madau (1995) to estimate the effective optical depth from the Lyman-series as a function of wavelength and redshift, which was coded into a local model for XSPEC. As well as estimating the hydrogen absorption caused by intervening systems, Madau (1995) also determined the error on this due to statistical fluctuations in the number of absorption clouds along the line of sight. This error was added in quadrature to the photometric uncertainty of any optical data at rest-frame wavelengths blueward of Lyα.

We found that the best-fitting models were consistent with there being no measurable dust in the host galaxy along the line of sight to the burst. Since many GRB host galaxies exhibit an SMC extinction law (Stratta et al. 2004; Kann et al. 2006; Starling et al. 2007; Schady et al. 2010) we adopted this for the fits to GRB 081029's SED. However, since the amount of fitted extinction is negligible ($A_V < 0.05$ mag at the 3-σ level, which is consistent with the upper limit derived in § 2.2), the details of the extinction law do not significantly affect our results. Our best-fitting models for each epoch are given in Table 4 for both a simple power law and a broken power law. The SEDs for all three epochs were fit simultaneously in both the simple power law case and the broken power law case. The extinction and H I column density were assumed to be the same at every epoch.

The simple power-law model assumes that the optical and X-ray photons are produced by the same mechanism. We find that the spectrum becomes steeper by $\Delta\beta = 0.19 \pm 0.02$ between ~ 3000 s and $12\,000$ s. This steepening occurs at about the same time that the light curve rebrightens indicating that there is a physical change in the mechanism that produces the light during the rebrightening. A broken power law provides a slightly better fit during the first epoch, but not at later times. We find that the spectrum has a break of $\Delta\beta = 0.67^{+1.59}_{-0.50}$ at $3.15^{+2.02}_{-0.83}$ keV at 3000 s (during the rebrightening). This steepening is consistent with a cooling break being located in the X-ray regime at this time. We also find that the optical spectrum becomes steeper between 5000 s and 9000 s, as is seen when fitting a single power-law spectrum.
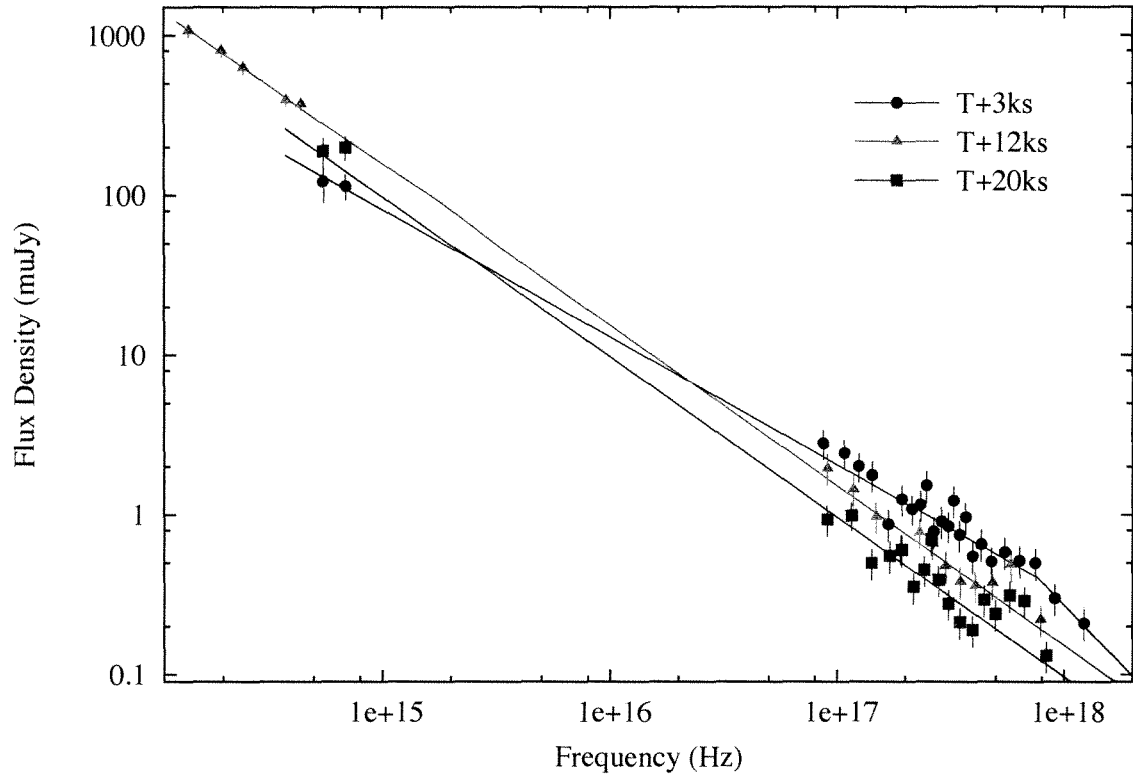
Fig. 7.— This Figure shows the best fit model SEDs to the optical, infrared, and X-ray data. The model is the SMC broken power law from Table 4. The fit at 3000 s is shown in black, the fit at 12 000 s is shown in red, and the fit at 20 000 s is shown in blue.

3.2. Light Curves

The flux light curves for the X-ray, optical, and infrared afterglows are presented in Figure 5. Between about 100 and 2000 s after the BAT trigger the REM optical data decays slowly with a decay index of $\alpha_{\mathrm{opt},1} = 0.52 \pm 0.02$. The ROTSE R-band data are consistent with a smooth decay with the same decay index. There is, however, considerable variation in the infrared luminosity during this period. Between about 3000 and 5000 s the X-ray light curve has a decay index of $\alpha_X = 0.56 \pm 0.03$. The optical light curve at this time, however, appears to be rising or flaring. Nardini et al. (2011) finds that the optical and infrared rose with $\alpha \sim -8$ during this period. Our data suggests that the optical flux peaks between ~ 5000 and $10\,000$ s and then fades with a decay index of $\alpha_{\mathrm{opt},2} = 1.89 \pm 0.25$. At $\sim 18\,000$ s the X-ray afterglow starts to decay steeply with $\alpha_{X,2} = 2.56 \pm 0.09$. This is steeper than the late-time optical decay ($\alpha_{\mathrm{opt},2} = 1.89 \pm 0.25$) at approximately the 2.5-σ level. However, we have very little optical data at late times, so it is possible that the observed optical decay is being affected by the mechanism that caused the brightening between 3000 and 5000 s.

4. Interpretation

4.1. The Synchrotron Peak

It is possible to interpret the brightening seen in the optical and infrared at about 3000 s as the synchrotron frequency passing though the optical on its journey towards lower energies. If the afterglow is in the fast cooling regime then the synchrotron peak frequency evolves as $\nu_m \propto t^{-1/2}$ (Sari et al. 1998). In this scenario the v band flux should peak ~ 2000–5000 s after the b band flux, depending on what time one takes for the peak in the v band. The times of the peaks in the v and b bands are very poorly constrained using our data, but it is possible that the b-band flux peaks before the v-band flux (but see Nardini et al. 2011). The expected index for the rising light curve before the synchrotron peak is -0.5, which is roughly consistent with what is seen in the b band ($\alpha \sim -0.8$). However, the rapid rise seen in the UVOT v band ($\alpha \sim -1.4$) and white band ($\alpha \sim -3.2$) are not consistent with the passage of the synchrotron frequency. Therefore, we conclude that the rise is not solely due to a synchrotron peak.

4.2. Energy Injection

The decay index of the X-ray light curve ($\alpha_{X,1} = 0.56$) up until about $18\,000$ s and the optical light curve ($\alpha_{\mathrm{opt},1} = 0.52$) up to about 2000 s are consistent with energy injection from ongoing central engine activity. We find an energy injection index of $q \sim 0.5$ where $L(t) \propto t^{-q}$ and an electron distribution index of $p \sim 2.7$ where $N(E) \propto E^p$. This scenario implies a homogeneous ISM and a cooling break that is above the X-ray band until at least $18\,000$ s (Zhang et al. 2006). This scenario fails, however, in that it predicts a late-time X-ray decay index of 1.75 (De Pasquale et al. 2009), which is significantly shallower than the observed value of $\alpha_{X,2} = 2.56$. It is possible that the energy injection ends at the same time as the jet break occurs ($\sim 18\,000$ s), but this requires an unlikely coincidence in the times of two events that are not physically connected to each other. Another reason for rejecting this scenario is that the late-time optical decay index is $\alpha_{\mathrm{opt}} = 1.89$, which is not consistent with either a jet break or the late-time X-ray decay index. Further, continuous energy injection cannot explain the jump in the flux seen at optical and infrared wavelengths at about 5000 s. Therefore, we conclude that continuous energy injection alone is not capable of explaining the light curves for this afterglow.

4.3. A Two-Component Jet

We are able to reproduce most of the observed X-ray, optical, and infrared light curves, as well as the observed spectral energy distribution if we assume a two-component jet model for the afterglow of GRB 081029. The afterglow is characterized by a rebrightening in the optical and infrared bands with a simultaneous flattening in the X-ray band. This implies that a new mechanism was contributing to the flux in the optical regime. In the two-component jet model, the early afterglow emission ($t < 2000$ s) was produced by the narrow, fast component while the late rebrightening was attributed to the emergence of the radiation powered by the wide, slow component.

In our fit the deceleration time for the wide component occurs earlier than 3000s, and we find that the synchrotron frequency of the wide jet compoment of the afterglow is between the X-ray and optical bands (i.e., $\nu_{\mathrm{opt}} < \nu_{\mathrm{m,w}} < \nu_X$) for $3000 < t < 9000$ s. The passage of the wide jet's synchrotron break through the optical band cannot reproduce the rapid rise that is seen in the optical and infrared photometry at about 3000 s, suggesting that there is another process at work that contributes to the sudden increase in the flux. Further, Nardini et al. (2011) find that optical flux rises as t^{-8} during this time.

The physical parameters of the two components are summarized in Table 5. The half-

opening angle of the jet is denoted by θ_j, Γ_0 is the Lorentz factor, $E_{K,\mathrm{iso}}$ is the isotropic equivalent kinetic energy in the jet, p is the electron index, ϵ_e and ϵ_B are the fractions of the energy in electrons and magnetic fields respectively, n is the density of the circumburst medium, and z is the redshift. Details of the model and the numerical code used are given in Jin et al. (2007).

We find that the narrow, inner jet has a half-opening angle of $\theta_{j,n} = 0.01$ rad and an initial Lorentz factor of $\Gamma_{0,n} = 500$. This component gives rise to the X-ray flux and the pre-jump optical and infrared flux. The wider, outer jet has $\theta_{j,w} = 0.02$ rad and an initial Lorentz factor of $\Gamma_{0,w} = 60$. This component dominates the afterglow after about $10\,000$ s. The total electromagnetic energy in the afterglow is approximately equally divided between the two jets.

Our two-component model predicts that the optical spectrum of the wide jet emission (which dominates at late time) has $\beta_{\mathrm{opt}} = 0.6$ and the X-ray spectrum has $\beta_X = 1.1$, with the break being located at $\sim 10^{15}$ Hz (approximately the u band), at ~ 9000 s This is not consistent with the fits to the observed SEDs presented in § 3.1. We tried varying the amount of extinction when fitting our models and found that the observed SEDs can be made to weakly agree with the model if there is extinction in the host galaxy along the line of sight to the burst. This is consistent with the constraints on the extinction ($A_V \lesssim 2$ mag in the host galaxy) from the X-ray data alone (§ 2.2) but inconsistent with the stronger constraint on the host extinction ($A_V < 0.03$ mag) found by combining the X-ray, optical, and infrared data (§ 3.1).

As a test of the two-component jet model we used the method of Molinari et al. (2007); Rykoff et al. (2009) to estimate the initial Lorentz factor of the narrow jet given the model parameters for our best-fitting narrow jet. To do this we assumed that the peak time of the narrow jet afterglow emission occured at or before the first ROTSE observations (at < 89 s after the BAT trigger), and an isotropic equivalent energy of 2.5×10^{54} erg (see Table 5), a radiative efficiency of $\eta = 0.2$ (Bloom et al. 2003), and a particle density of $n_0 = 10$ cm^{-2} (see Table 5). This gives an estimated lower limit on the initial Lorentz factor of $\gtrsim 500$, which is consistent with the model value that we find for the narrow jet ($\Gamma_{0,n} = 500$).

As shown in Figure 8 the two-component jet model can reproduce the X-ray and some of the optical/infrared data reasonably well, but fails to reproduce the rapid rise seen in the UVOT white data. Further, GROND observations show that this rapid rise occurs in all filters between the GROND $g\prime$ and K_s bands and has a power law index of $\alpha \sim -8$ (Nardini et al. 2011). This is steeper than can be accomodated with the two-component jet model. We conclude that the two-component jet model can explain all of the observed features of the afterglow except the sudden rebrightening.
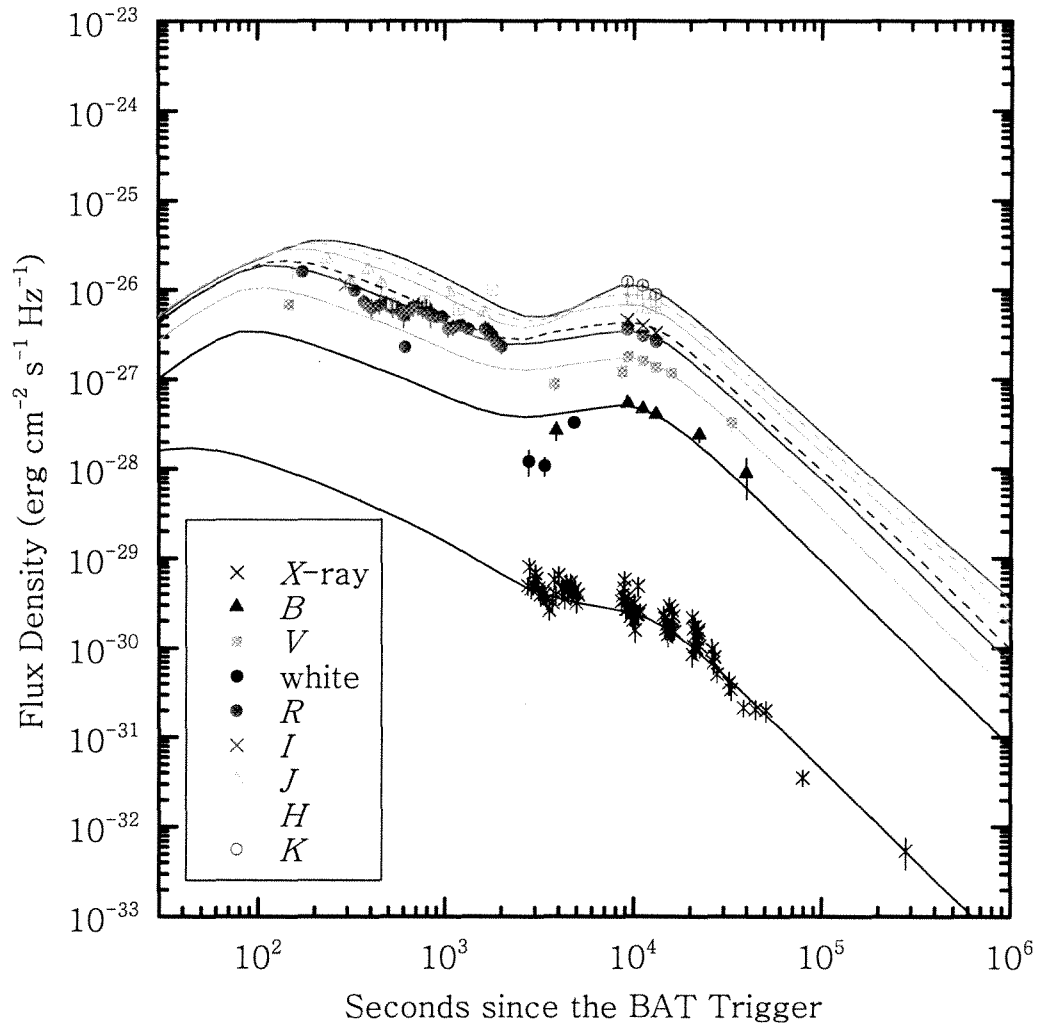
Fig. 8.— This Figure shows the best-fitting two-component jet model for our light curves. The colours used in the Figure are the same as in Figure 5.

4.4. Colliding Shells

Continuing central engine activity is not able to explain the observed light curves without having to assume that the energy injection ends at the same time that the jet break occurs. It is also unable to explain the jump seen at ~ 3000 s. However, Vlasis et al. (2011) have proposed that collisions between ejecta shells can produce flares in the optical light curve. In their scenario the first shell sweeps up a uniform insterstellar medium and decelerates. The second shell has a higher Lorentz factor and overtakes the first shell. The collision between the two shells produces an optical flare with properties that depend on the Lorentz factor of the second shell and the isotropic energy (E_{iso}). They find that the collision between the two shells of material with different Lorentz factors can produce an optical flare with $\Delta t/t \sim 1$. The lack of data between ~ 3000 and ~ 9000 s makes it difficult to determine $\Delta t/t$ for the rebrightening of the optical afterglow of GRB 081029. However, the v and b photometry suggests that the flare had a duration of between roughly 5000 s and 10 000 s, and peaked between roughly 5000 s and 9000 s. This suggests that $(\Delta t/t) \sim 1$, which is consistent with the prediction of the colliding shell scenario. The simulations of Vlasis et al. (2011) suggest that the magnitude of the flare, relative to the underlying synchrotron light curve, depends on the Lorentz factor and the isotropic energy. They find typical values for the increase in the flux (f) resulting from the collision of $\Delta f/f \sim 2$–5 for typical GRB values of Γ and E_{iso}. This is consistent with what is seen for GRB 081029.

Figures 4 and 5 of Vlasis et al. (2011) show the predicted optical light curves produced by colliding ejecta shells for four sets of Lorentz factor and isotropic energy. All four cases result in light curves that exhibit flares that have similar shapes and intensities as what is seen in GRB 081029. The simulations assume $\Gamma = 23$ for the first shell, which results in the onset of a flare at $\sim 20 000$ in the rest frame. Our data suggest that the GRB 081029's flare started at ~ 3000 s in the observer's frame (~ 600 s in GRB 081029's rest frame). However, the time of the collision will depend on the time that the second (faster) shell was ejected relative to the first (slower) shell, and on the distance of the first shell from the central engine (and the first shell's Lorentz factor). Detailed simulations will be needed to test this scenario and determine the physical properties of the ejecta.

The colliding shell scenario can explain the fast rise seen in the optical data, but it does not address the shallow decay seen in the optical before about 2000 s or the shallow X-ray decay during the optical rise.

5. Discussion

5.1. The Afterglow

In general we find that by themselves neither a one-component jet nor continuous energy injection from the central engine can explain the observed light curves and spectral energy distribution of the X-ray, optical, and infrared afterglows of GRB 081029. A two-component jet model, similar to what is seen in some other GRB afterglows, does provide a reasonable fit to the light curves, but cannot reproduce the rapid rise in the flux seen in the UVOT white filter, nor can it explain the rapid rise seen in the GROND light curves (Nardini et al. 2011). Further, the two-component jet model is not able to reproduce the observed SEDs during the unusual optical activity.

We find that the rise in the optical light curves of the afterglow of GRB 081029 can be broadly explained by the collision of a fast-moving ejecta shell with a slower shell that has been decelerated by sweeping up a uniform insterstellar medium. This scenario does not, however, address the shallow decay phase of the afterglow. The early shallow decay requires either continuous energy injection from the central engine or a multi-component jet. We favour the multi-component jet explaination because it does not require energy injection to end at the same time that an (unrelated) jet break occurs. The discrepancy between the observed SED (with $\beta = 1$ and $A_V < 0.05$ mag) and the SED that is predicted by by the two-jet model (with $\beta = 0.6$ and $A_V \sim 0$ mag) can be explained by the spectrum at $\sim$ 9000 s being dominated by emission from the flare caused by the collision between the two shells. Evidence for this is that at 3000 s, during the onset of the flare, the SED had $\beta = 0.8$, which suggests a transition between the intrinsic SED of the narrow jet and the SED of the emission from the collision. If this is the case there is no need to invoke extinction to explain the difference between the observed and predicted spectral decay indices. This leads to a picture where GRB 081029 had a two-component jet and a collision between two ejecta shells at about 3000 s. At this time the afterglow is making a transition from being dominated by the narrow jet to being dominated by the wide jet, so it is not possible to tell if the collision between the two ejecta shells occured in the narrow or wide jet.

The nature of GRB afterglows has been a matter of much debate over the past decade. There is a general agreement that they are the result of a combination of a forward shock due to a relativistic jet moving into the circumstellar medium surrounding the burst and a reverse shock that propagates back into the jet. However, the details of how these shocks affect their environment, the role of magnetic fields, and the structure of the jets are the subject of much research. Several GRBs have had afterglows that are difficult or impossible to explain using a single, uniform jet. A multi-component jet structure has been postulated to explain unusual

behaviour in the light curves of some GRBs. An example of a multi-component jet is given by Berger et al. (2003), who invoked a two-component jet to explain radio observations of the long–soft burst GRB 030329. Oates et al. (2007) found that a two-component jet explained GRB 050802's afterglow, and Holland et al. (2007) found that a two-component jet could explain the lack of a jet break in the light curves of XRF 050416A. Racusin et al. (2008) found that the afterglow emission from the "naked-eye burst" GRB 080319B is best explained using a two-component jet. A multi-component jet can also explain the afterglow of the short–hard burst GRB 051221A (Jin et al. 2007). However, the physical parameters of multi-component jets vary considerably from one GRB to another, so there does not appear to be a universal jet structure.

Multi-component or structured jets are predicted by simulations of the relativistic outflow from GRBs. Kumar & Granot (2003) found that the bulk Lorenz factor decreases as one moves away from the axis of the jet resulting in a jet with a fast inner core surrounded by a slower outer envelope. Simulations of outflows from accretion discs about collapsed massive stars show that multi-component jets can form with the outer jet carrying far more energy than the inner jet (Vlahakis et al. 2003). In this scenario the inner and outer jet will have different energies and different bulk Lorentz factors. The interaction of each jet with the circumburst medium will produce separate afterglow emission components, which can result in complex light curves (Peng et al. 2005).

Several mechanisms have been proposed to create late-time activity in the central engine of a GRB that would result in multiple ejecta events. King et al. (2005) suggest that the fragmentation of a rapidly-rotating stellar core could result in multiple accretion events onto the newly-formed compact object. Perna et al. (2006) pointed out that the fragmentation of an accretion disc that is undergoing viscous evolution can result in an accretion disc that results in highly variable accretion onto the central compact object. Each accretion event would restart the central engine resulting in new shells being ejected. Each accretion event would be independent, so the initial Lorentz factors of the ejecta could vary considerably leading to collisions between shells from different events.

There is evidence for colliding shells in the optical light curves of a few GRBs. The afterglow of GRB 081029 has an optical light curve that is similar to that of GRB 060206 (Stanek et al. 2007; Woźniak et al. 2006), and GRB 970508 (Sokolov et al. 1998) exhibited a late-time flare similar to what is expected from colliding shells. After ten years such flares have only been observed in a handful of GRB afterglows, which suggests that discrete late-time accretion events may be fairly uncommon in GRBs.

A combination of the colliding shell scenario and a multi-component jet can reproduce the broad features of the light curves, but detailed modelling will be needed to determine the

physical parameters governing this afterglow. Several GRB afterglows have shown evidence for multi-component jets, and there is evidence that some GRBs undergo multiple accretion events that result in late-time impulsive energy injection into the afterglow. GRB afterglows appear to be complex phenomena that require detailed modelling to be fully understond.

5.2. The Host Galaxy

We detect both hydrogen absorbing features (Lyα and Lyβ) and several metallic transitions in the spectrum of the optical afterglow. The latter belong both to neutral elements (O I(1039) and (1302)), low ionization species (C II(1334), S II(1250), (1253), and (1259), Si II(1264), (1304), and (1526), Fe II(1608), Al II(1670), Al III(1854)) and high ionization species (N V(1238) and (1242), Si IV(1393) and (1402), C IV(1548) and (1550), O VI(1031) and (1037)). In addition to these features, lines from several fine structure levels of C II(1334), O I(1304) and (1306), Si II(1264), (1309), and (1533), and Fe II(1618), (1621), (1631), and (1636) are detected. These features are excited by the ultraviolet flux from the GRB afterglow. Estimates of the typical distance from a GRB to absorption systems suggest distances of $\sim$ 0.1–1 kpc (Vreeswijk et al. 2007; D'Elia et al. 2009) implying that all these absorption features are due to the GRB 081029 host galaxy. The common redshift of these features is $z = 3.848$, which we take at the redshift of the host. We find no evidence for intervening metal absorption lines in our combined spectrum.

6. Conclusions

GRB 081029 was a long–soft GRB with a redshift of $z = 3.8479$. It had a smooth gamma-ray light curve and did not appear to have any unusual gamma-ray properties. Neither the gamma-ray nor the X-ray properties of this burst showed any sign of strange behaviour. The optical and infrared light curves, on the other hand, were not typical of GRB afterglows. There was a brightening in the optical and infrared light curves at about 3000 s that cannot be explained as the passage of the synchrotron break through the optical, by a two-component jet model, or by continuous energy injection from the central engine. We find that the combination of the colliding shell scenario of Vlasis et al. (2011) and a two-component jet can reproduce the unusual optical light curve of this afterglow. Our result is consistent with a central engine that was reactivated by a discrete, major accretion event.

REFERENCES

Ballester, P., Modigliani, A., Boitquin, O., Cristiani, S., Hanischik, R., Kaufer, A., & Wolf, S., 2000, ESO Messenger, 101, 31

Barthelmy, S. D., Barbier, L. M., Cummings, J. R., Fenimore, E. E., Gehrels, N., Hullinger, D., Krimm, H. A., Markwardt, C. B., et al., 2005, Sp. Sci. Rev., 120, 143

Berger, E., Kulkarni, S. R., Pooley, G., Frail, D. A., McIntyre, V., Wark, R. M., Sari, R., Soderberg, A. M., Fox, D. W., Yost, S., & Price, P. A., 2003, Nature, 426, 154

Bertin, E. & Arnouts, S., 1996, A&AS, 117, 393

Bessell, M. S., 1990, PASP, 102, 1181

Bessell, M. S., Castelli, F., & Plez, B., 1998, A&A, 333, 231

Beuermann, K., Hessman, F. V., Reinsch, K., Nicklas, H., Vreeswijk, P. M., Galama, T. J., Roll, E., van Paradijs, J., et al., 1999, A&A, 352, L26

Bloom, J. S., Frail, D. A., & Kulkarni, S. R., 2003, ApJ, 594, 674

Breeveld, A. A., Curran, P. ., Hoversten, E. A., Koch, S., Landsman, W., Marshall, F. E., Page, M. J., Poole, T. S., 2010, MNRAS, 406, 1687

Burrows D. N., Hill, J. E., Nousek, J. A., Kennea, J. A., Wells, A. A., Osborne, J. P., Abbey, A. F., Beardmore, A., et al., 2005, Sp. Sci. Rev. 120, 165

Chincarini, G., Zerbi, F. M., Antonelli, A., Conconi, P., Cutispoto, G., Covino, S., D'Alessio, F., de Ugarte Postigo, A., et al., 2003, The Messenger, 113, 40

Clemens, C., Loew, S., & Greiner, A., 2008, GCNC 8437

Cobb, B. E., 2008, GCNC 8452

Cohen, M., Walker, R. G., Barlow, M. J., & Deacon, J. R., 1992a, AJ, 104, 1650

Cohen, M., Walker, R. G., & Witteborn, F. C., 1992b, AJ, 104, 2030

Covino, S., Covino, S., Antonelli, L. A., Malesani, D., Fugazza, D., Calzoletti, L., Campana, S., Chincarini, G., et al., 2008, GCNC 8441

Covino, S., Stefanon, M., Sciuto, G., Fernandez-Soto, A., Tosti, A. G., Zerbi, F. M., Chincarini, G., Antonelli, L. A., et al., 2004, SPIE, 5492, 1613

Cucchiara, A., Fox, D. B., Cenko, S .B., & Berger, E., 2008, GCNC 8448

Cummings, J. R., Barthelmy, S. D., Baumgartner, W. H., Fenimore, E. E., Gehrels, N., Krimm, H. A., Markwardt, C. B., Palmer, D. M., et al., 2008, GCNC 8447

D'Elia, V., Covino, S., & D'Avanzo, P, 2008, GCNC 8438

D'Elia, V., Fiore, F., Perna, R., Krongold, Y., Covino, S., Fugazza, D., Lazzati D., Nicastro, F., et al., 2009, ApJ, 694, 332

Dekker, H., D'Odorico, S., Kaufer, A., Delabre, B., & Kotzlowski, H., 2000, SPIE, 4008, 534

De Pasquale, M., Evans, P., Oates, S., Page, M., Zane, S, Schady, P., Breeveld, A., Holland, S. T., et al., 2009, MNRAS, 392, 153

Evans, P. A., Beardmore, A. P., Page, K. L., Tyler, L. G., Osborne, J. P., Goad, M. R., O'Brien, P. T., Vetere, L., et al., 2007, A&A, 469, 379

Fey, A. L., Ma, C., Arias, E. F., Charlot, P., Feissel-Vernier, M., Contier, A.-M., Jacobs, C. S., & MacMillan, D. S., 2004, AJ, 127, 3587

Gehrels, N., Chincarini, G., Ciommi, P., Mason, K. O., Nousek, J. A., Wells, A. A., White, N. E., Barthelmy, S. D., et al., 2004, ApJ, 611, 1005

Goad, M. R., Osborne, J. P., Beardmore, A. P. & Evans, P. A., 2008, GCNC 8443

Holland, S. T. & Sakamoto, T., 2008, GCNC 8450

Holland, S. T., Boyd, P. T., Gorosabel, J., Hjorth, J., Schady, P., Thomsen, B., Augusteijn, T., Blustin, A. J., et al., 2007, AJ, 113, 122

Jin, Z.-P., Yan, T., Fan, Y.-Z., & Wei, D. M., 2007, ApJ, 656, L57

Kalberla, P. M. W., Burton, W. B., Hartmann, D., Arnal, E. M., Bajaja, E., Morras, R., & Pöppel, W. G. L., 2005, A&A, 440, 77

Kann, D., Klose, S., & Zeh, A., 2006, ApJ, 641, 993

King, A., O'Brien, P. T., Goad, M. R., Osborne, J., Olsson, E., & Page, K. 2005, ApJ, 630, L113

Kumar, P., & Granot, J., 2003, ApJ, 591, 1075

Madau, P., 1995, ApJ, 441, 18

Moin, A., Tingay, S., Phillips, C., Taylor, G., Wieringa, M., & Martin, R., 2008, GCNC 8634

Molinari, E., Vergani, S. D., Malesani, D., Covino, S., D'Avanzo, P. D., Chincarini, G., Zerbi, F. M., Antonelli, L. A., et al., 2007, A&A, 469, L13

Nardini, M., et al., 2011, GRB 2010 Proceedings, eds, J. McEnery, J. Racusin, & N. Gehrels, in press

Oates, S. R., De Pasquale, M., Page, M. J., Blustin, A. J., Zane, S. McGowan, K., Mason, K. O., Poole, T. S., et al., 2007, MNRAS,380, 270

Pei, Y. C., 1992, ApJ, 395, 130

Peng, F., Kömigl, A., & Granot, J., 2005, ApJ, 626, 966

Perna, R., Armatige, P. J., & Zhang, B., 2006, ApJ, 636, L29

Poole,T. S., Breeveld, A. A., Page, M. J., Landsman, W., Holland, S. T., Roming, P., Kuin, N. P. M., Brown, P. J., et al., 2008, MNRAS, 383, 627

Quimby, R. M., Rykoff, E. S., Yost, S. A., Aharonian, F., Akerlof, C. W., Alatalo, K., Ashley, M. C. B., Göğüş, E., et al., 2006, ApJ, 640, 402

Racusin, J. L., Karpov, S. V., Sokolowski, M., Granot, J., Wu, X. F., Pal'Shin, V., Covino, S., van der Horst, A. J., et al., 2008, Nature, 455, 183

Roming, P. W. A., Koch, T. S., Oates, S. R., Porterfield, B. L., Vanden Berk, D. E., Boyd, P. T., Holland, S. T., Hoversten, E. A., et al., 2009, ApJ, 690, 163

Roming, P. W. A., Kennedy, T. E., Mason, K. O., Nousek, J. A., Ahr, L., Bingham, R. E., Broos, P. S., Carter, M. J., et al., 2005, Sp. Sci. Rev., 120, 95

Rykoff, E. S., 2008, GCNC 8436

Rykoff, E. S., Aharonian, F., Akerlof, C. W., Ashley, M. C. B., Barthelmy, S. D., Flewelling, H. A., Gehrels, N., Göğüş, E., et al., 2009, ApJ, 702, 489

Sakamoto, T., Baumgartner, W. H., Burrows, D. N., Gehrels, N., Gronwall, C., Guidorzi, C., Holland, S. T., Krimm, H. A., et al., 2008, GCNC 8435

Sakamoto, T., Barthelmy, S. D., Berbier, L., Cummings, J. R., Fenimore, E. E., Gehrels, N., Hullinger, D., Krimm, H. A., et al., 2008, ApJS, 175, 179

Sari, R., Piran, T., & Narayan, R. 1998, ApJ, 497, L17

Schady, P., Page, M. J., Oates, S. R., Still, M., De Pasquale, M., Dwelly, T.,Kuin, N. P. M., Holland, S. T., et al., 2010, MNRAS, 401, 2773

Schady, P., Mason, K. O., Page, M. J., De Pasquale, M., Morris, D. C., Romano, P., Roming, P. W. A., Immler, S., et al., 2007, MNRAS, 377, 273

Schlegel, D. J., Finkbeiner, D. P., & Davis, M., 1998, ApJS, 500, 525

Sokolov, V. V., Kopulov, A. I., Zharikov, S. V., Feroci, M., Nicastro, L., Palazzi, E., 1998, A&A, 334, 117

Stanek, K. Z., Dai, X., Prieto, J. L., Garnavich, P. M., Calkins, M. L., Severn, J., Worthey, G., Hao, H., et al., 2007, ApJ, 654, L21

Starling, R. L. C., Wijers, R. A. M. J., Wiersema, K., Rol, E., Corran, P. A., Kouveliotou, C., van der Holst, A. J., & Heemskerk, M. H. M., 2007, ApJ, 661, 787

Stratta, G., Fiore, F., Piro, L., & De Pasquale, M., 2004, ApJ, 608, 846

Ukwatta, T. N., Sakamoto, T., Stamatikos, M., Gehrels, N., & Dhuga, K. S., in AIP Conf. Proc. 1000, Gamma-Ray Bursts 2007, eds. M. Galassi, D. Palmer & E. Fenimore, (arXiv:0802.3815)

Vlahakis, N., Peng, F., & Kønigl, A., 2003, ApJ, 594, L23

Vlasis, A., van Eerten, H. J., Meliani, Z., & Keppens, R., 2011, MNRAS, in press, arXiv:1103.2936

Vreeswijk, P. M., Ledoux, C., Smette, A., Ellison, S. L., Jaunsen, A. O., Andersen, M. L., Fruchter, A. S., Fynbo, J. P. U., et al., 2007, A&A, 468, 83

Woźniak, P. R., Vestrand, W. T., Wren, J. A., White, R. R., Evans, S. M., Casperson, D., 2006, ApJ, 642, L99

Zerbi, F. M., Chincarini, G., Ghisellini, G., Rondonó, M., Tosti, G., Antonelli, L. A., Conconi, P., Covino, S., et al., 2001, AN, 322, 275

Zhang, B., Fan, Y. Z., Dyks, J., Kobayashi, S., Mészaáros, P., Burrows, D. N., Nousek, J. A., & Gehrels, N., 2006, ApJ, 642, 354

Table 1. The photometry of GRB 081029. These data have not been corrected for either Galactic extinction or any possible extinction in the host galaxy. The first column is the midpoint time of the observation in seconds since the BAT trigger (2008 Oct 29 at 01:43:56 UT). The second column is the filter name while the third column is the total exposure time in seconds. The fourth and fifth columns give the magnitudes and associated 1-sided 1-σ statistical errors. The sixth and seventh columns give the flux and its 2-sided 1-σ statistical error in erg cm^{-2} s^{-1}. The upper limits are 3-σ upper limits.

Time (s)	Filter	Exposure (s)	Magnitude	Error	Flux	Error
3788	v	197	19.04	$-0.19, +0.23$	1.394×10^{-13}	0.027×10^{-13}
6941	v	200	18.69	$-0.20, +0.25$	1.916×10^{-13}	0.383×10^{-13}
15711	v	885	18.74	$-0.09, +0.09$	1.834×10^{-13}	0.157×10^{-13}
32934	v	885	20.13	$-0.19, +0.23$	0.516×10^{-13}	0.101×10^{-13}
3890	b	393	20.46	$-0.22, +0.28$	0.830×10^{-13}	0.190×10^{-13}
22201	b	514	20.58	$-0.17, +0.20$	0.740×10^{-13}	0.124×10^{-13}
39638	b	318	21.67	$-0.42, +0.71$	0.271×10^{-13}	0.130×10^{-13}
2784	white	147	20.51	$-0.30, +0.41$	1.576×10^{-13}	0.494×10^{-13}
3377	white	197	20.65	$-0.22, +0.28$	1.383×10^{-13}	0.324×10^{-13}
4813	white	197	19.43	$-0.10, +0.10$	4.251×10^{-13}	0.389×10^{-13}

Table 2. REM observation log for GRB 081029. Magnitudes are not corrected for reddening.

Mid Obs. Time (UT)	$t - t_0$ (s)	Exposure (s)	Instrument	Mag	Filter
20081029.07814	515	23.0	REM/REMIR	15.41 ± 0.17	H
20081029.08122	781	35.5	REM/REMIR	15.34 ± 0.08	H
20081029.08590	1185	61.0	REM/REMIR	15.57 ± 0.05	H
20081029.09291	1791	86.0	REM/REMIR	15.04 ± 0.02	H
20081029.07396	154	36.0	REM/REMIR	15.09 ± 0.10	J
20081029.07488	233	35.5	REM/REMIR	14.66 ± 0.07	J
20081029.07579	312	35.5	REM/REMIR	15.31 ± 0.12	J
20081029.07671	391	35.5	REM/REMIR	14.95 ± 0.09	J
20081029.07748	458	23.5	REM/REMIR	15.32 ± 0.24	J
20081029.08437	1053	61.0	REM/REMIR	15.57 ± 0.08	J
20081029.09079	1608	85.5	REM/REMIR	16.16 ± 0.09	J
20081029.07600	330.048	1×30.0	REM/ROSS	16.25 ± 0.15	R
20081029.07646	369.792	1×30.0	REM/ROSS	16.57 ± 0.21	R
20081029.07692	409.536	1×30.0	REM/ROSS	16.72 ± 0.24	R
20081029.07737	448.416	1×30.0	REM/ROSS	16.66 ± 0.22	R
20081029.07782	487.296	1×30.0	REM/ROSS	16.61 ± 0.21	R
20081029.07828	527.040	1×30.0	REM/ROSS	16.74 ± 0.24	R
20081029.07873	565.920	1×30.0	REM/ROSS	16.78 ± 0.25	R
20081029.07918	604.800	1×30.0	REM/ROSS	16.94 ± 0.29	R
20081029.07964	644.544	1×30.0	REM/ROSS	16.81 ± 0.25	R
20081029.08009	683.424	1×30.0	REM/ROSS	16.71 ± 0.23	R
20081029.08054	722.304	1×30.0	REM/ROSS	16.69 ± 0.23	R
20081029.08101	762.912	1×30.0	REM/ROSS	16.77 ± 0.24	R
20081029.08146	801.792	1×30.0	REM/ROSS	16.71 ± 0.23	R
20081029.08191	840.672	1×30.0	REM/ROSS	16.94 ± 0.29	R
20081029.08253	894.240	1×60.0	REM/ROSS	16.98 ± 0.16	R
20081029.08334	964.224	1×60.0	REM/ROSS	16.97 ± 0.16	R
20081029.08414	1033.344	1×60.0	REM/ROSS	17.31 ± 0.21	R
20081029.08494	1102.464	1×60.0	REM/ROSS	17.27 ± 0.21	R
20081029.08609	1201.824	1×120.0	REM/ROSS	17.21 ± 0.11	R
20081029.08758	1330.560	1×120.0	REM/ROSS	17.32 ± 0.12	R
20081029.09108	1632.960	1×60.0	REM/ROSS	17.33 ± 0.22	R
20081029.09187	1701.216	1×60.0	REM/ROSS	17.38 ± 0.23	R
20081029.09269	1772.064	1×60.0	REM/ROSS	17.51 ± 0.26	R
20081029.09383	1870.560	1×120.0	REM/ROSS	17.71 ± 0.18	R
20081029.09532	1999.296	1×120.0	REM/ROSS	17.81 ± 0.19	R

Table 3.   ROTSE observation log for GRB 081029. Magnitudes are not corrected for reddening.

$t - t_0$ (s)	Mag	$-$Err	$+$Err
89.220435	15.92	-0.17	+0.20
97.120160	16.03	-0.15	+0.18
105.019280	15.99	-0.17	+0.20
112.919869	16.02	-0.14	+0.17
120.819853	15.89	-0.12	+0.14
128.719663	16.20	-0.15	+0.18
136.619302	16.13	-0.17	+0.20
144.619942	16.16	-0.19	+0.23
152.619718	15.87	-0.20	+0.24
160.518838	16.20	-0.15	+0.18
187.520268	16.26	-0.11	+0.13
216.818422	15.96	-0.13	+0.15
246.219132	16.50	-0.16	+0.19
275.619497	16.80	-0.19	+0.23
304.420246	16.52	-0.19	+0.22
333.519507	16.56	-0.21	+0.26
362.620064	16.96	-0.26	+0.34
391.818339	16.72	-0.17	+0.20
421.219913	16.95	-0.17	+0.20
450.419052	16.99	-0.21	+0.26
499.120182	16.89	-0.13	+0.15
568.520118	16.92	-0.14	+0.17
637.619728	16.74	-0.13	+0.15
706.619372	17.01	-0.14	+0.16
775.719846	16.96	-0.17	+0.20
844.720355	16.97	-0.15	+0.18
913.719308	17.12	-0.18	+0.22
982.318489	17.03	-0.14	+0.16
1051.019967	17.39	-0.16	+0.18
1120.119318	17.70	-0.22	+0.27
1500.119642	17.57	-0.08	+0.09
2190.069070	17.96	-0.16	+0.19
2880.419956	18.47	-0.23	+0.29
3570.918956	18.42	-0.24	+0.32
60256.035925	>19.61	$\cdots$	$\cdots$

Table 4. Model fits to the combined optical and X-ray SEDs. The A_V values are 3-σ upper limits.

Epoch	A_V (mag)	N_H (10^{21} cm^{-2})	β_1	β_2	$E_{\rm bk}$ (keV)
SMC Single Power Law: $\chi^2/{\rm DoF} = 59.4/54 = 1.10$					
3000	< 0.05	$8.70^{+2.77}_{-2.50}$	0.81 ± 0.02	$\cdots$	$\cdots$
12 000			1.00 ± 0.01	$\cdots$	$\cdots$
20 000			1.03 ± 0.03	$\cdots$	$\cdots$
SMC Broken Power Law: $\chi^2/{\rm DoF} = 58.1/51 = 1.14$					
3000	< 0.03	$8.87^{+2.76}_{-2.51}$	$0.80^{+0.02}_{-0.03}$	$1.47^{+1.59}_{-0.50}$	$3.15^{+2.02}_{-0.83}$
12 000			1.00 ± 0.01	$\cdots$	$\cdots$
20 000				$\cdots$	$\cdots$

Table 5. Model fits for a two-component jet.

Parameter	Narrow Jet	Wide Jet
θ_j (rad)	0.01	0.02
Γ_0	500	60
$E_{K,\rm iso}$ (erg)	2.5×10^{54}	2.0×10^{54}
p	2.2	2.2
ϵ_e	0.02	1/3
ϵ_B	0.0002	0.0002
n (cm^{-3})	10	10
z	3.8479	3.8479